

Preprint PFC/JA-83-20

END EFFECTS OF A BIFILAR MAGNETIC WIGGLER

J. Fajans

Plasma Fusion Center and
Research Laboratory of Electronics
Massachusetts Institute of Technology
Cambridge, MA. 02139

June 1983

End Effects of a Bifilar Magnetic Wiggler

J. Fajans

Department of Physics and Research Laboratory of Electronics
Massachusetts Institute of Technology
Cambridge, MA 02139

Abstract

The magnetic field at the entrance of a wiggler magnet in a Free Electron Laser (FEL) determines the character of the electron orbits and influences the FEL gain. To obtain the desired adiabatic entrance conditions, it is necessary to investigate different methods of connecting leads to the wiggler as well as methods of gradually reducing the wiggler field. The field of a current driven, finite length bifilar helical wiggler magnet is derived and is used to investigate the magnetic field end perturbations. For a limited range of wiggler parameters, flaring the wiggler end produces an adiabatic entrance region. Alternately, gradually terminating the wiggler current at the wiggler entrance is shown to produce an adiabatic entrance for a larger range of parameters.

Section 1—Introduction

Free electron laser gain is dependent on the quality of the electron orbits. A poor quality, high temperature beam will force an FEL from the Raman towards the Compton regime, substantially reducing the gain of the device.¹ Several authors have shown that beam quality is dependent on the magnetic field profile at the entrance of the wiggler.^{2,3,4} The formula for the field of a current driven, infinitely long bifilar helical wiggler is, in cylindrical coordinates (Fig. 1)^{5,6}

$$\mathbf{B} = -\frac{2ik_\lambda b\mu_0}{\pi} \nabla \left\{ \sum_{p=1}^{\infty} \sin \frac{p\pi}{2} \cos p(\phi - k_\lambda z) K'_p(pk_\lambda b) I_p(pk_\lambda r) \right\}, \quad (1)$$

where I and K are modified Bessel functions,⁷ i is the current, $k_\lambda = 2\pi/\lambda$, λ is the wiggler period, and b is the radius of the helix. The appearance⁴ of large magnetic field spikes at the ends of finite wigglers obviously cannot be predicted by this formula. In the section 2 of this paper, an exact expression is derived for the magnetic field of a finite length wiggler magnet. End effect magnetic field spikes are discussed in the third section. The entrance field profile is often tailored by flaring the windings outward at the end of the wiggler magnet. This technique and its limits are discussed in the section 4. An alternate method of tailoring the magnetic field is to gradually decrease the current at the end of the wiggler by inserting current dividers every half period. Section 5 discusses this method, which is valid over a larger parameter regime than the flaring method.

Section 2—Finite Length Wiggler Field

The magnetic field of a finite length bifilar wiggler magnet can be represented as a magnetic scalar potential expressed as a Fourier-Bessel series. If the current in the windings of a wiggler is assumed to flow in a current sheet of current density K at radius $r = b$, then the wiggler field can be found by applying appropriate boundary conditions to a scalar magnetic potential. Using the standard \gtrless notation with $<$ denoting the solid cylindrical region $0 \leq r < b$ and $>$ denoting the hollow cylindrical region $b \leq r < \infty$, then

$$\mathbf{B} = -\nabla \Phi_{\gtrless}, \quad \nabla^2 \Phi_{\gtrless} = 0 \quad (2)$$

where Φ_{\gtrless} satisfies the boundary condition for the normal and tangential field components:

$$\hat{r} \cdot \nabla (\Phi_{>} - \Phi_{<})|_{r=b} = 0 \quad (3)$$

$$-\hat{r} \times \nabla (\Phi_{>} - \Phi_{<})|_{r=b} = \mu_0 K. \quad (4)$$

The general solution to Laplace's equation in cylindrical coordinates (r, ϕ, z) is⁸ (Fig. 1)

$$\Phi_{\gtrless} = \sum_{\nu\mu} \left(A_{\nu\mu}^{\gtrless} \sin \mu\phi \sin \nu z + B_{\nu\mu}^{\gtrless} \sin \mu\phi \cos \nu z + C_{\nu\mu}^{\gtrless} \cos \mu\phi \sin \nu z + D_{\nu\mu}^{\gtrless} \cos \mu\phi \cos \nu z \right) \mathcal{R}_{\mu}^{\gtrless}(\nu r), \quad (5)$$

where

$$\mathcal{R}_\mu^>(\nu r) \equiv K_\mu(\nu r), \quad \mathcal{R}_\mu^<(\nu r) \equiv I_\mu(\nu r)$$

and where I and K are modified Bessel functions. Periodicity in ϕ implies that μ is restricted to integers values. If the system is assumed to have a spatial period k , equation (5) can be rewritten

$$\begin{aligned} \Phi_{>} = \sum_{nm} \left(A_{nm}^> \sin m\phi \sin nkz + B_{nm}^> \sin m\phi \cos nkz \right. \\ \left. + C_{nm}^> \cos m\phi \sin nkz + D_{nm}^> \cos m\phi \cos nkz \right) \mathcal{R}_m^>(nkr). \end{aligned} \quad (6)$$

In cylindrical coordinates, the boundary condition (3) implies

$$0 = \sum_{nm} nk (A_{nm}^> K'_m(nkr) - A_{nm}^< I'_m(nkr)) \sin m\phi \sin nkz |_{r=b}, \quad (7)$$

or

$$A_{nm}^> = \frac{I'_m(nkb)}{K'_m(nkb)} A_{nm}^< \quad (8)$$

with similar equations for B , C , and D . Assuming that the current in the current sheet can be represented in a Fourier series of the form

$$\begin{aligned} K = \sum_{nm} (A_{nm} \sin m\phi \sin nkz + B_{nm} \sin m\phi \cos nkz \\ + C_{nm} \cos m\phi \sin nkz + D_{nm} \cos m\phi \cos nkz), \end{aligned} \quad (9)$$

and, using the Wronskian for modified Bessel functions, the boundary condition (4) becomes

$$\begin{aligned} \mu_0 K = \hat{z} \sum_{nm} \frac{m}{b} \frac{1}{nkb K'_m(nkb)} (-A_{nm} \cos m\phi \sin nkz - B_{nm} \cos m\phi \cos nkz \\ + C_{nm} \sin m\phi \sin nkz + D_{nm} \sin m\phi \cos nkz) \\ + \hat{\phi} \sum_{nm} \frac{1}{b K'_m(nkb)} (A_{nm} \sin m\phi \cos nkz - B_{nm} \sin m\phi \sin nkz \\ + C_{nm} \cos m\phi \cos nkz - D_{nm} \cos m\phi \sin nkz). \end{aligned} \quad (10)$$

Once the coefficients for the current density A , B , C , and D , are known, the above boundary condition can be readily used to determine the scalar potential coefficients A , B , C , and D .

For an infinite wiggler it is generally assumed that the current in the current sheet flows in infinitesimally thin wires that can be represented by ⁹

$$\vec{K} = ik_\lambda \left(\hat{\phi} + \frac{\hat{z}}{k_\lambda b} \right) \delta(r-b) \sum_{j=-\infty}^{\infty} \left[\delta\left(\phi - k_\lambda z + \frac{\pi}{2} + 2\pi j\right) - \delta\left(\phi - k_\lambda z - \frac{\pi}{2} + 2\pi j\right) \right] \quad (11)$$

where i is the current, $k_\lambda = 2\pi/\lambda$ and λ is the wiggler period. Since the current is divergenceless, the finite wiggler current circuit must include the wiggler termination. The total current is divided into two components, with the wiggler component K_w representing the current in the

helical windings, and with the termination component K_t representing the current due to a loop termination between the two wires in the helix (Figure 2). For computational simplicity a periodic system of wigglers is assumed, each wiggler having a length of $2M\lambda$ and a center to center separation of $2N\lambda$ (Figure 3). Thus the system spatial period k is equal to $k_\lambda/2N$. With these definitions the current becomes:

$$K = K_t + K_w \quad (12)$$

where

$$K_t = i\hat{\phi}\delta(r-b)\left(u\left(\phi + \frac{\pi}{2}\right) - u\left(\phi - \frac{\pi}{2}\right) - \frac{1}{2}\right) \times \sum_{h=-\infty}^{\infty} (\delta(z - (l + 2Lh)) - \delta(z - (-l + 2Lh))) \quad (13)$$

$$K_w = ik_\lambda\left(\hat{\phi} + \frac{\hat{z}}{k_\lambda b}\right)\delta(r-b) \sum_{h=-\infty}^{\infty} [u(z - (-l + 2Lh)) - u(z - (l + 2Lh))] \times \sum_{j=-\infty}^{\infty} \left[\delta\left(\phi - k_\lambda z + \frac{\pi}{2} + 2\pi j\right) - \delta\left(\phi - k_\lambda z - \frac{\pi}{2} + 2\pi j\right)\right], \quad (14)$$

and u is the unit step function, $L = N\lambda$ and $l = M\lambda$.

Evaluation of the termination component K_t is straightforward. By symmetry, $A_{nm}^t = B_{nm}^t = D_{nm}^t = 0$, and

$$C_{nm}^t = \frac{4i\hat{\phi}}{m\pi L} \sin \frac{n\pi M}{N} \sin \frac{m\pi}{2}. \quad (15)$$

The integrals for the wiggler components are standard, but involved. For example,

$$A_{nm}^w = \frac{i}{\pi L} \left(\hat{\phi} + \frac{\hat{z}}{k_\lambda b}\right) \left(\sum_{j=-M+1}^{M-1} \int_{-\pi}^{\pi} d\phi \sin m\phi \left[\sin \frac{n}{2N} \left(\phi + \frac{\pi}{2} + 2\pi j\right) - \sin \frac{n}{2N} \left(\phi - \frac{\pi}{2} + 2\pi j\right) \right] \right. \\ \left. + \int_{-\pi}^{-\pi/2} d\phi \sin m\phi \sin \frac{n}{2N} \left(\phi + \frac{\pi}{2} + 2\pi M\right) \right. \\ \left. - \int_{-\pi}^{\pi/2} d\phi \sin m\phi \sin \frac{n}{2N} \left(\phi - \frac{\pi}{2} + 2\pi M\right) \right. \\ \left. + \int_{-\pi/2}^{\pi} d\phi \sin m\phi \sin \frac{n}{2N} \left(\phi + \frac{\pi}{2} - 2\pi M\right) \right. \\ \left. - \int_{\pi/2}^{\pi} d\phi \sin m\phi \sin \frac{n}{2N} \left(\phi - \frac{\pi}{2} - 2\pi M\right) \right). \quad (16)$$

These integrals were evaluated using the symbolic manipulation program Macsyma.¹⁰ The answers are

$$A_{nm}^w = D_{nm}^w = 0, \quad B_{nm}^w = \frac{n}{2N} \mathcal{G}_{nm}, \quad C_{nm}^w = -m \mathcal{G}_{nm}$$

$$G_{nm} = \frac{i}{\pi L} \left(\hat{\phi} + \frac{\hat{z}}{k_\lambda b} \right) \frac{4}{m^2 - n^2/4N^2} \sin \frac{m\pi}{2} \sin \frac{n\pi M}{N}. \quad (17)$$

Using the boundary condition (10) to match the coefficients of K to the coefficients in Φ and rearranging the terms gives

$$\Phi = \sum_{nm} \left[e_{nm} \cos(m\phi - \frac{n}{2N} k_\lambda z) + f_{nm} \cos(m\phi + \frac{n}{2N} k_\lambda z) \right] I_m(\frac{n}{2N} k_\lambda r), \quad (18)$$

with

$$e_{nm} = \frac{1}{m - n/2N} h_{nm} \quad f_{nm} = \frac{-1}{m + n/2N} h_{nm}$$

$$h_{nm} = \frac{2i\mu_0}{\pi L} \frac{n/2N}{m} b K'_m(\frac{n}{2N} k_\lambda b) \sin \frac{m\pi}{2} \sin \frac{n\pi M}{N}.$$

The magnetic field is then found by using (2).

Section 3—End Effects

In numerical examples the field obtained from (18) was checked with the results obtained from the Biot-Savart law. Figure 4 gives the on-axis field for two typical examples. Note that for $b/\lambda = .5$, the end spike magnitude is only about thirty percent greater than the wiggler amplitude, while for $b/\lambda = 1$ the end spike magnitude is about five times larger than the wiggler amplitude. Figure 5 graphs the Fourier coefficients for a typical wiggler. The infinite wiggler would have a single non-zero coefficient corresponding to a spatial frequency of $k = k_\lambda$; instead in the finite case there is a distribution of spatial frequencies around k_λ and another, new set of spatial frequencies around $k = \pi/N\lambda \approx 0$.

The graphs of the wiggler field clearly show a large spike at the end of the wiggler. This spike has two sources; (a) the loop termination at $z = 0$ (Figure 2) contributes:¹¹

$$\mathbf{B} = -\frac{\mu_0 i}{2\pi} \frac{bz}{(b^2 + z^2)^{3/2}} \hat{x}. \quad (19)$$

The large $\pm z$ limit for \mathbf{B} is

$$\mathbf{B} = \mp \frac{\mu_0 i}{2\pi} \frac{b}{z^2} \hat{x}. \quad (20)$$

The second spike source is (b) the lack of helical symmetry at the end of the wiggler. This contribution may be investigated with the formula

$$\mathbf{B} = \frac{\mu_0 i}{4\pi} \int_0^\infty d\theta \frac{2b}{(z_e^2 + b^2)^{(3/2)}} \left\{ \hat{x} \left[z_e \sin \theta - \frac{1}{k_\lambda} \cos \theta \right] - \hat{y} \left[\frac{1}{k_\lambda} \sin \theta + z_e \cos \theta \right] \right\}_{z_e = z - \frac{e}{k_\lambda}} \quad (21)$$

which represents the on-axis field of an unterminated wiggler extending from $z = 0$ to $z = \infty$. In the limit of large $-z$ this equation converges to

$$B_z \approx -\frac{\mu_0 i b}{2\pi z^2}. \quad (22)$$

Since the \hat{x} contributions from the unterminated wiggler and from the loop termination are equal and opposite in the limit of large z , the end spike in the \hat{x} direction is much smaller than might otherwise be expected.

Another plausible termination is to extend each wire to $\pm\infty$ (Figure 6); this termination contributes:

$$\mathbf{B} = -\frac{\mu_0 i}{2\pi z} \left[1 - \frac{b}{\sqrt{b^2 + z^2}} \right] \hat{x}. \quad (23)$$

This termination does not possess the appropriate large z limit and results in a much larger spike in the \hat{x} direction. Figure 7 compares the fields due to the two types of terminations.

Without the cancellation from the loop termination, the spike in the \hat{x} direction is larger than the spike in the \hat{y} direction. With the loop termination, the \hat{y} spike is dominant. In the limit of large z , (21) shows that B_y goes to zero as the inverse third power of z . However this limit is only valid where B_y is negligible. At $z = 0$, (21) can be evaluated for B_y exactly:¹²

$$B_y = 2\frac{\mu_0}{4\pi} i b k_\lambda^2 \left\{ \frac{\pi}{2} [I_0(k_\lambda b) - L_0(k_\lambda b)] + \frac{\pi}{2k_\lambda b} [I_1(k_\lambda b) - L_{-1}(k_\lambda b)] - \frac{1}{k_\lambda b} \right\}, \quad (24)$$

where L_ν is a modified Struve function.⁷ The small b/λ limit is

$$B_y = -\frac{\mu_0}{\pi} i k_\lambda \left\{ 1 - \frac{3}{8}\pi k_\lambda b + \frac{2}{3}(k_\lambda b)^2 - \frac{5}{64}\pi(k_\lambda b)^3 \dots \right\}. \quad (25)$$

The large b/λ limit can be expressed as an asymptotic series in inverse powers of b/λ . Since the position of the maximum in B_y is very close to the end of the wiggler, an accurate sense of the end spike magnitude can be found by evaluating these formulas for B_y at $z = 0$.

The strength of an infinite wiggler is

$$|\mathbf{B}| \approx \frac{\mu_0 i b k_\lambda^2}{\pi} K'_1(k_\lambda b), \quad (26)$$

and since $k_\lambda b$ is usually greater than unity, $|\mathbf{B}|$ is proportional to $\exp(-k_\lambda b)$. However, (24) shows that for b/λ greater than one, the end spike decreases as an inverse power of b . Thus the ratio of the end spike amplitude to the wiggler amplitude increases exponentially for large b/λ . This ratio is graphed in Figure 8.

Section 4—Flared Wigglers

The wiggler entrance field can be shaped by flaring the winding radius b outwards as a function of z at the entrance of the wiggler magnet. Since $|\mathbf{B}|$ is proportional to $\exp(-k_\lambda b)$, if b is increased from some b_1 in the central, constant magnitude section of the wiggler to

$$b_f \approx b_i - \frac{1}{k_\lambda} \ln R \quad (27)$$

at the end of the wiggler, then the ratio of the end field strength to the central field strength is approximately R . Clearly the radius must not be increased too rapidly, or the helical symmetry of the wiggler will be destroyed. Without helical symmetry in the flare, the wiggler will effectively terminate at the small, $b \approx b_i$ end of the flare, and the spiral character of the wiggler field in the entrance region will be lost.

Even when the radius is increased slowly, the range of values of b_i for which this technique is effective is limited by the end spike discussed in Section 3. For values of b_f/λ greater than one, the end spike will mask the desired wiggler field. Thus in order to achieve a large wiggler amplitude reduction factor R the constant radius section of the wiggler must have a value of b_i/λ small enough so that the value of b_f/λ , as defined by (27), is less than one. Since b_i/λ is often not small, this condition effectively limits the size of the the wiggler amplitude reduction factor R . Figure 9a graphs the field of a flared wiggler with an appropriately small value of b_i/λ , while Figure 9b graphs the field of flared wiggler with a larger value of b_i/λ . In both cases $R = 1/100$ and b_f was determined by (27). The figures show that even when the b_f/λ condition is met, there is still a significant perturbation at the end of the wiggler. Increasing the number of periods in the flare does not remove the problem.

Section 5—Staggered Termination Wigglers

By slowly decreasing the current at the wiggler end, the magnetic field can be made to follow a desired profile. Loop terminators like those shown in Figure 2 inserted every half period are used to reduce the current in discrete steps. The configuration is drawn in Figure 10. The fraction of the current terminated in each loop, and the consequent entrance magnetic field profile, are controlled by individual external loads. If the impedance of each load is greater than the impedance of a half period of the wiggler¹³, the current in each termination loop can be adjusted freely. Typically a reactance of ten milli-ohms is sufficient. The fields from a wiggler with a six period termination region for two different values of b/λ are shown in Figure 11. This method works so long as the wiggler meets the criterion that b/λ is less than one. Since there is no flare, this criterion is much less restrictive than in the case of a flared wiggler. Advantages of this method include smooth, adjustable field profiles, and ease of fabrication.

Section 6—Conclusions

The field of a finite wiggler has a number of undesirable features not present in an infinite wiggler. Careful attention to the wiggler end region and to the wiggler termination is necessary to mitigate these features. For a limited range of wiggler configurations, flaring the wiggler end outward produces an adequately smooth entrance. Gradually decreasing the wiggler current at the wiggler end produces a smooth entrance over a wider range of parameters.

Acknowledgments

This work was supported in part by the National Science Foundation and in part by the Hertz Foundation. Macsyma is supported by NASA, ONR, DOE, and USAF.

References

- ¹ Kroll, N., W. McMullin, *Phys. Rev. A.* 17, 300 (1978).
- ² Friedland, L., *Phys. Fluids.* 23, 2376 (1980).
- ³ Fajans, J., G. Bekefi, B. Lax, *IEEE Conference on Plasma Science, Ottawa.* (May 17-19, 1982).
- ⁴ Vallier, L., J.M. Buzzi, *Bull. American Physical Society.* 27, 8 (Oct. 1982).
- ⁵ Kincaid, B., *J. Appl. Phys.* 48, 2684 (1977).
- ⁶ Blewett, J., R. Chasman, *J. Appl. Phys.* 48, 2692 (1977).
- ⁷ *Handbook of Mathematical Functions*, Abramowitz, M., I. Stegun, eds. National Bureau of Standards, Washington, (1972).
- ⁸ Jackson, J.D., *Classical Electrodynamics*, Wiley, New York, 107 (1975).
- ⁹ Diament, P., *Physical Review A.* 23, 2539 (1981).
- ¹⁰ Pavelle, R., et al, *Scientific American.* 245, 130 (1981).
- ¹¹ Buzzi, J.M., K. Felch, & L. Vallier, *Etude du Champ Magnetique Produit par une Double Helice*, PMI 1008, Laboratoire de Physique des Milieux Ionises, Ecole Polytechnique, France, (1980).
- ¹² Gradshteyn, I.S., I.M. Ryzhik, *Table of Integrals, Series, and Products*, Academic Press, New York, 426 (1980).
- ¹³ Fajans, J., *Bifilar Wiggler Inductance*, Plasma Fusion Center Report number PFC/JA-82-21, Massachusetts Institute of Technology, Cambridge, MA, (1982).

Figure 1. Cylindrical Coordinate Space, (r, ϕ, z)

Current flows only in a current sheet at $r = b$.

Figure 2. Loop Termination Wiggler



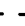
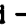

Helical windings are   , and , Loop Termination is .

Figure 3. Wiggler System

Every wiggler has $2M$ periods, and the wiggler centers are separated by $2N\lambda$.

Figure 4a. Wiggler End Fields

$B_x = \text{---}$, $B_y = \text{---}$, $\lambda = 3.3\text{cm}$, $b = 1.65\text{cm}$. Note that the B_y end spike is larger than the B_x end spike. With $b/\lambda = .5$, the magnitude of the spike is 30 percent larger than the magnitude of the wiggler.

Figure 4b. Wiggler End Fields

$B_x = \text{---}$, $B_y = \text{---}$, $\lambda = 3.3\text{cm}$, $b = 3.3\text{cm}$. With $b/\lambda = 1$, the magnitude of the end spike is 5 times greater than the magnitude of the wiggler.

Figure 5a. e_{n1}, f_{n1} vs. n

Normalized $m = 1$ Fourier coefficients for a typical wiggler. $\bullet = e_{n1}$, $\blacksquare = f_{n1}$, $\lambda = 3.3\text{cm}$, $b = 2\text{cm}$. The peak in f_{n1} for large n contains the infinite wiggler terms. All other terms are due to the finite length of the wiggler.

Figure 5b. e_{nm} vs. n, m

Normalized Fourier coefficients for a typical wiggler.

Figure 6. Lead Termination Wiggler

Helical windings are — — —, and ———, Lead Termination is ———.

Figure 7. B_z vs. z for two types of terminations

———— = Loop Termination Wiggler, — — — = Lead Termination Wiggler. The Lead Termination Wiggler suffers from a larger end spike and a slowly decaying bias.

Figure 8. End Spike normalized by wiggler magnitude vs. b/λ

■ = \hat{x} spike, • = \hat{y} spike. The \hat{y} spike is larger than the \hat{x} end spike and grows exponentially for b/λ greater than one.

Figure 9a. B vs. z for a flared wiggler.

B_x = — — —, B_y = ———, $|B|_{\text{actual}}$ = — · — · —, $|B|_{\text{desired}}$ = — · · — · · —, $\lambda = 3.3\text{cm}$, final $b = .55\text{cm}$, entrance $b = 2.97\text{cm}$. The flare satisfies the condition $b/\lambda < 1$. The field follows the desired linearly increasing field reasonably well with a discrepancy at the beginning of the flare of about ten percent.

Figure 9b. B vs. z for a flared wiggler.

B_x = — — —, B_y = ———, $|B|_{\text{actual}}$ = — · — · —, $|B|_{\text{desired}}$ = — · · — · · —, $\lambda = 3.3\text{cm}$, final $b = 1.65\text{cm}$, entrance $b = 4.06\text{cm}$. The flare does not satisfy the condition $b/\lambda < 1$. The end discrepancy is about thirty percent.

Figure 10a. Staggered Termination Wiggler

Helical windings are — — —, and ———, Terminations are ———.

Figure 10b. Staggered Termination Wiggler Equivalent Circuit

Z_w is half the impedance of a half period of the wiggler, Z_t is the impedance of each terminator, and Z_{L_n} is the impedance of the external load of terminator n . By adjusting each Z_{L_n} , the currents i_n can be controlled. For simplicity, the helix has been untwisted.

Figure 11a. B vs. z for a Staggered Termination Wiggler

$B_x = \text{---} \text{---} \text{---}$, $B_y = \text{---}$, $|B|_{\text{actual}} = \text{---} \cdot \text{---} \cdot \text{---}$, $\lambda = 3.3\text{cm}$, $b = .55\text{cm}$.

Figure 11b. B vs. z for a Staggered Termination Wiggler

$B_x = \text{---} \text{---} \text{---}$, $B_y = \text{---}$, $|B|_{\text{actual}} = \text{---} \cdot \text{---} \cdot \text{---}$,

$\lambda = 3.3\text{cm}$, $b = 1.65\text{cm}$. The field follows the desired linearly increasing field with no major discrepancies. The ripple in the increasing wiggler magnitude is about three percent of the final wiggler magnitude.

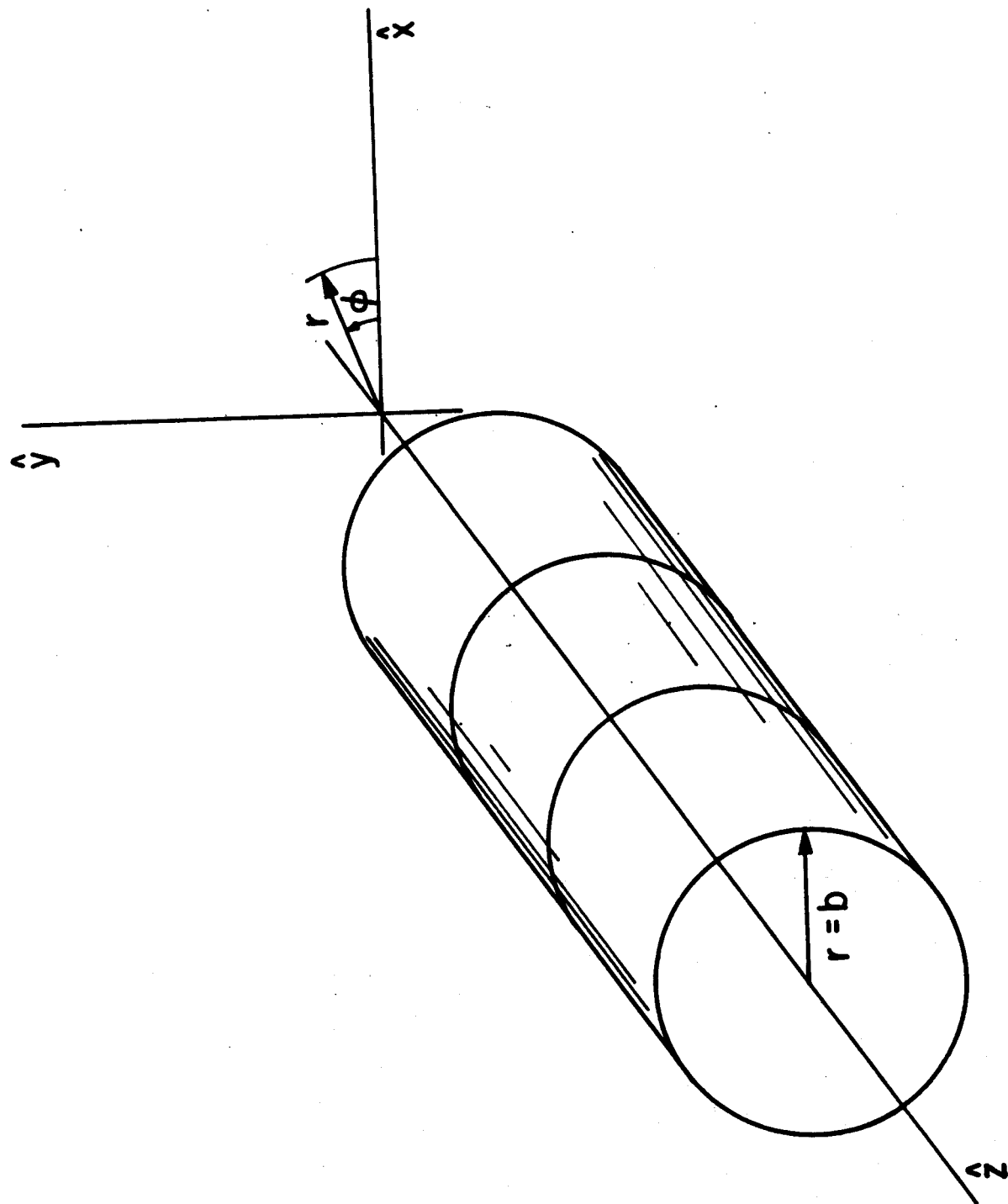


Fig. 1
Fajans

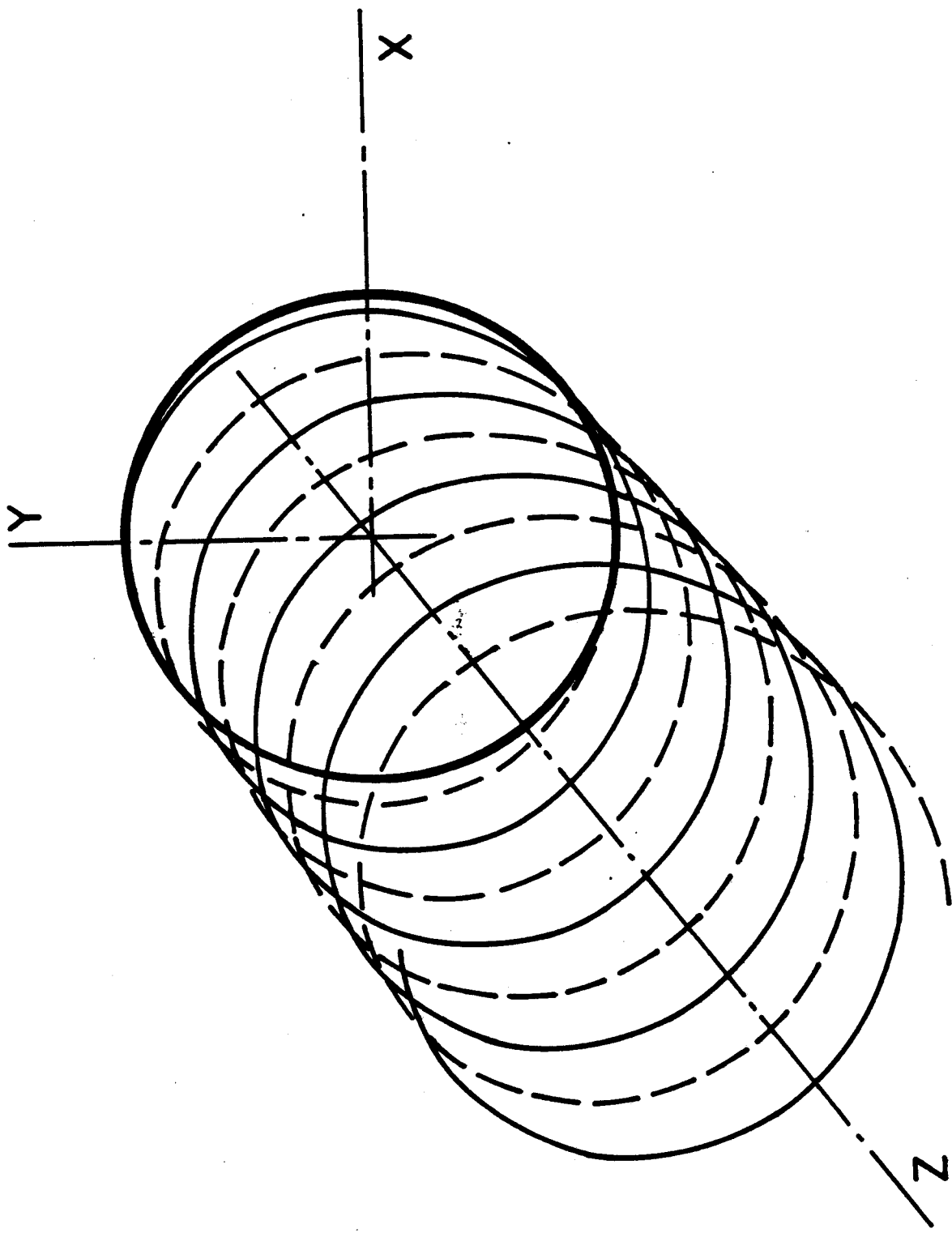


Fig. 2
Fajans

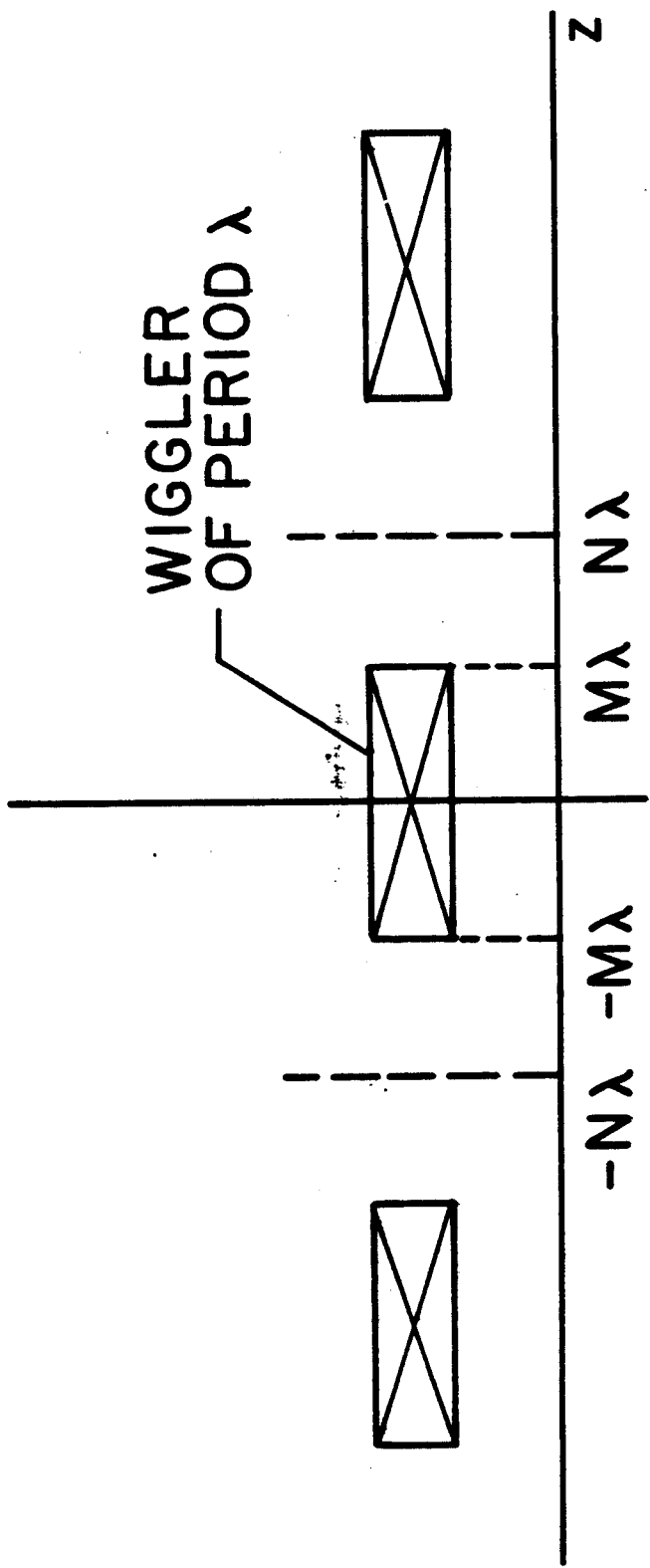


Fig. 3
Fajans

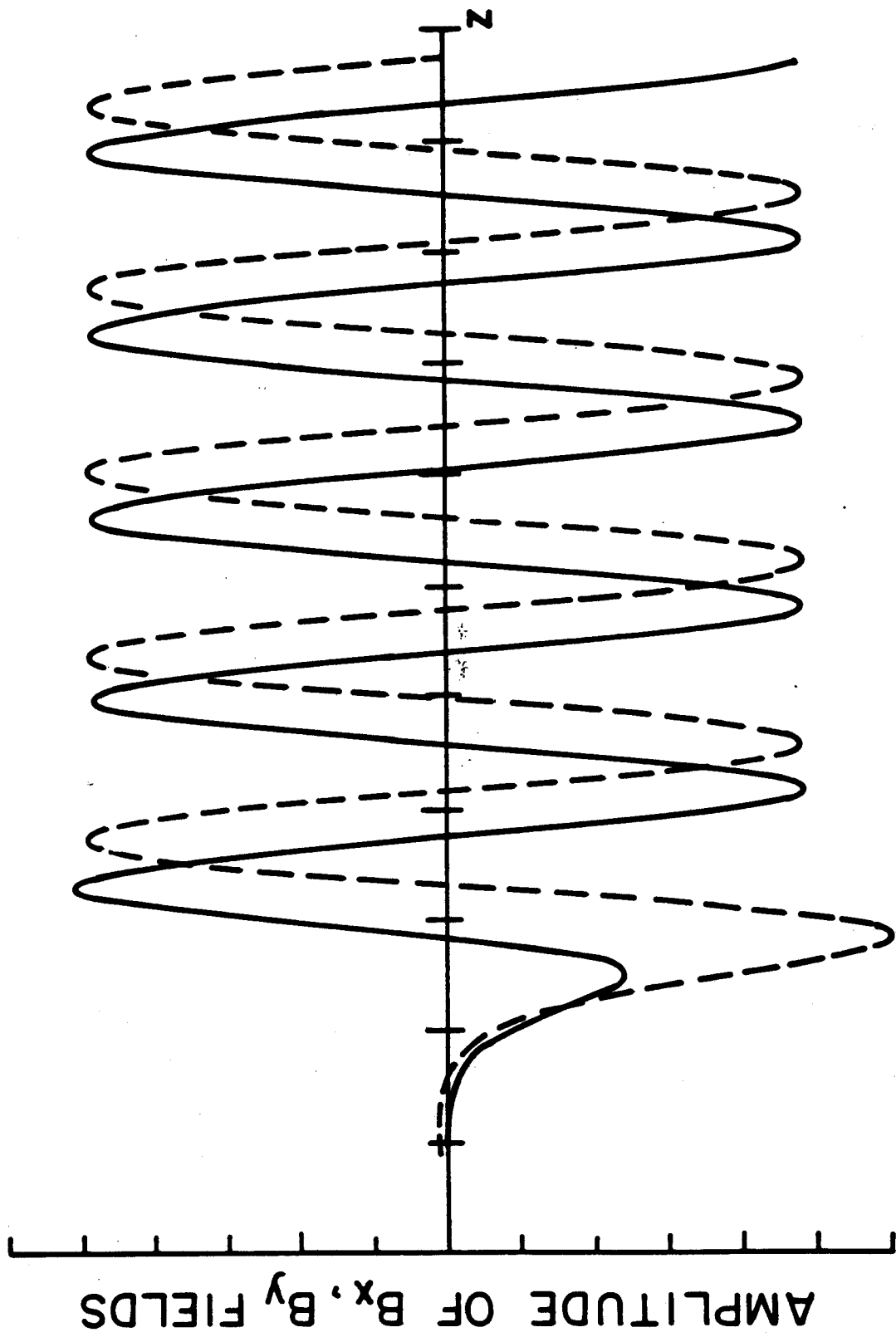


Fig. 4a
Fajans

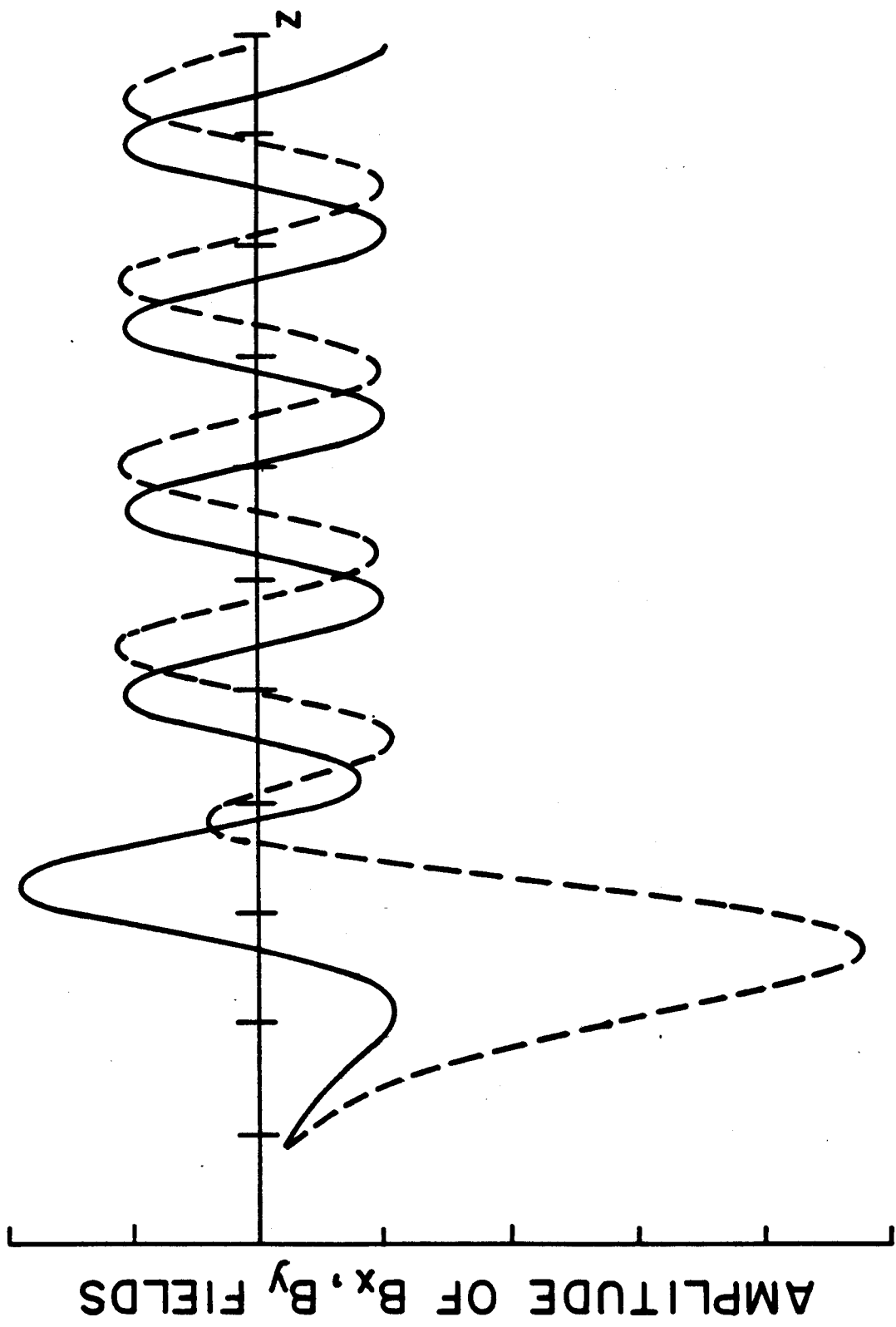
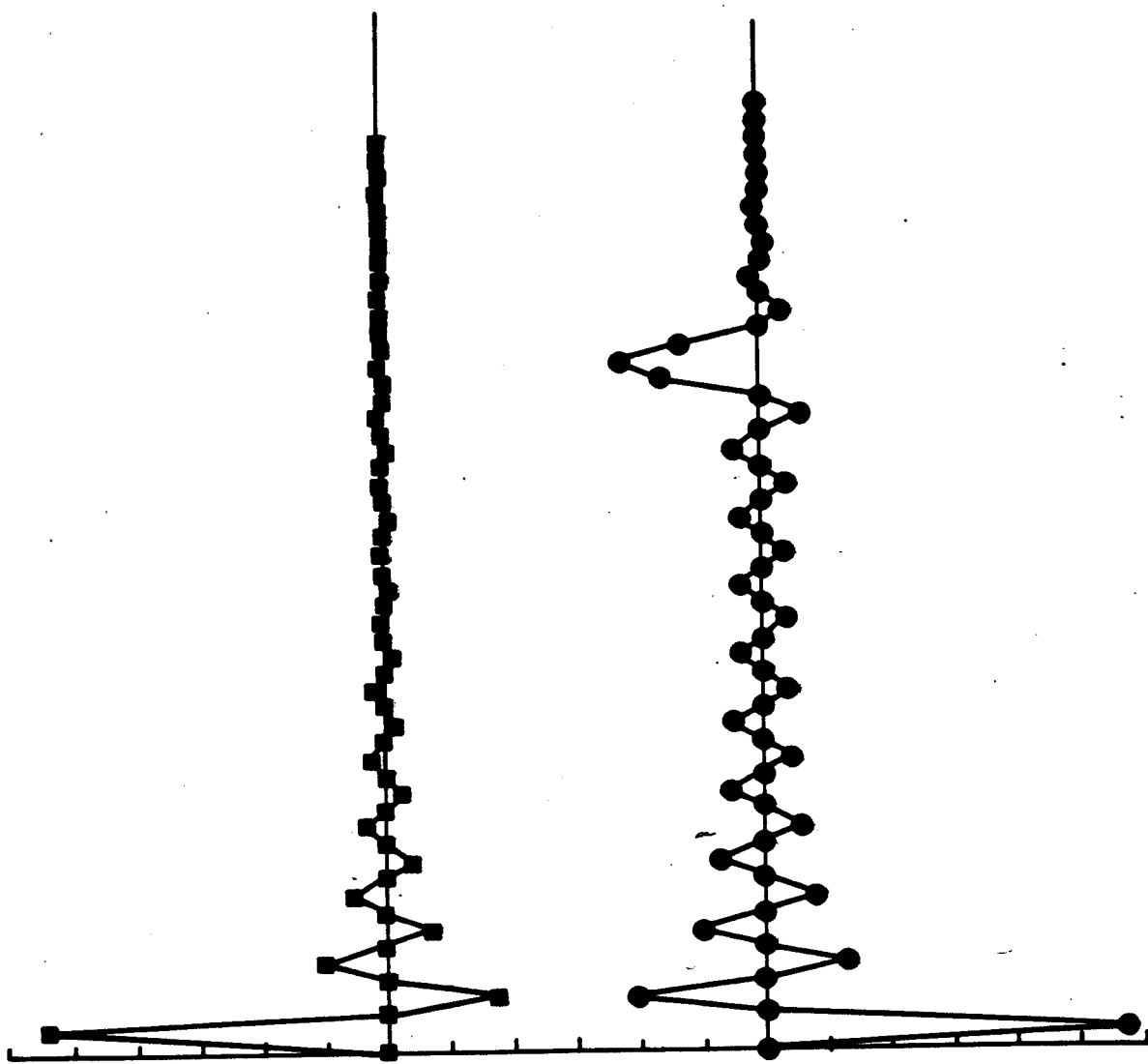


Fig. 4b
Fajans

Fig. 5a
Fajans



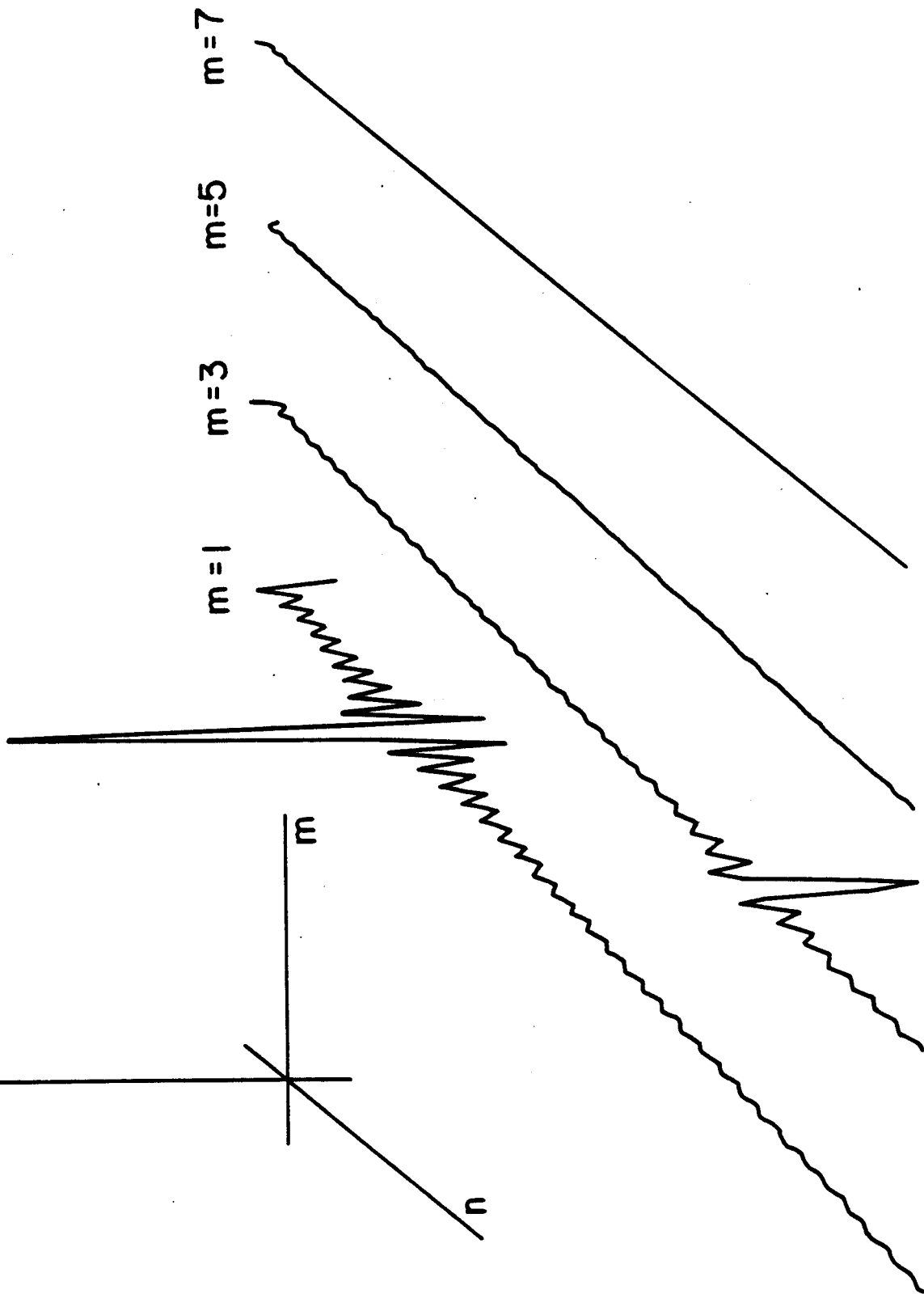
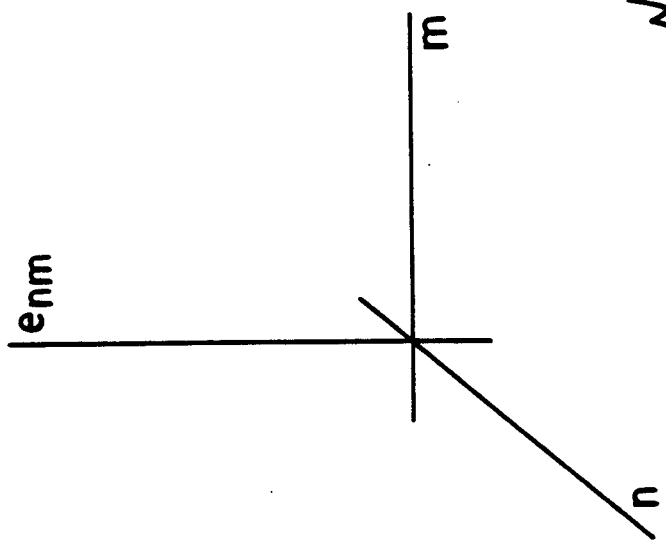


Fig. 5b
Pajans

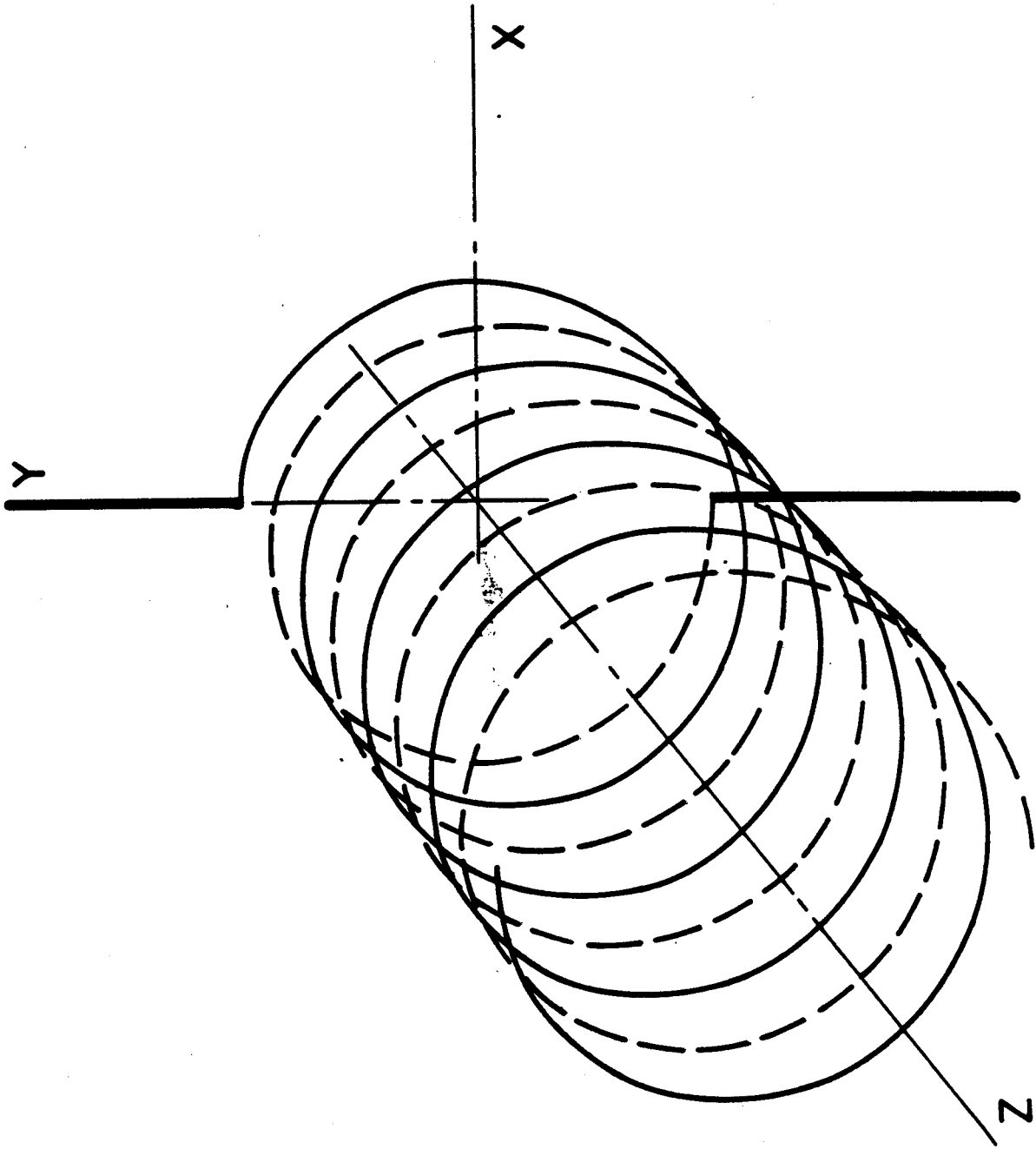


Fig. 6
Fajans

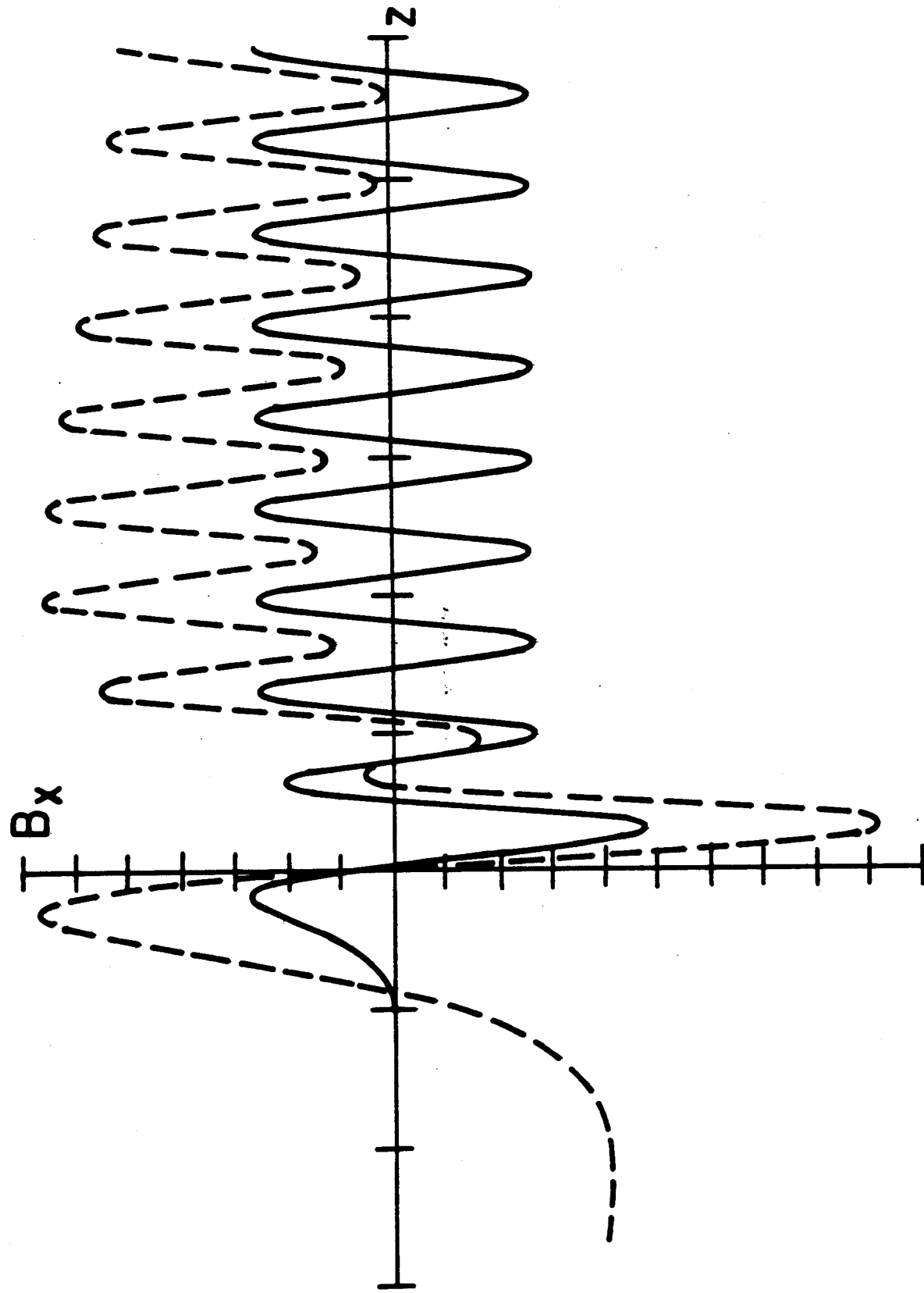


Fig. 7
Fajans

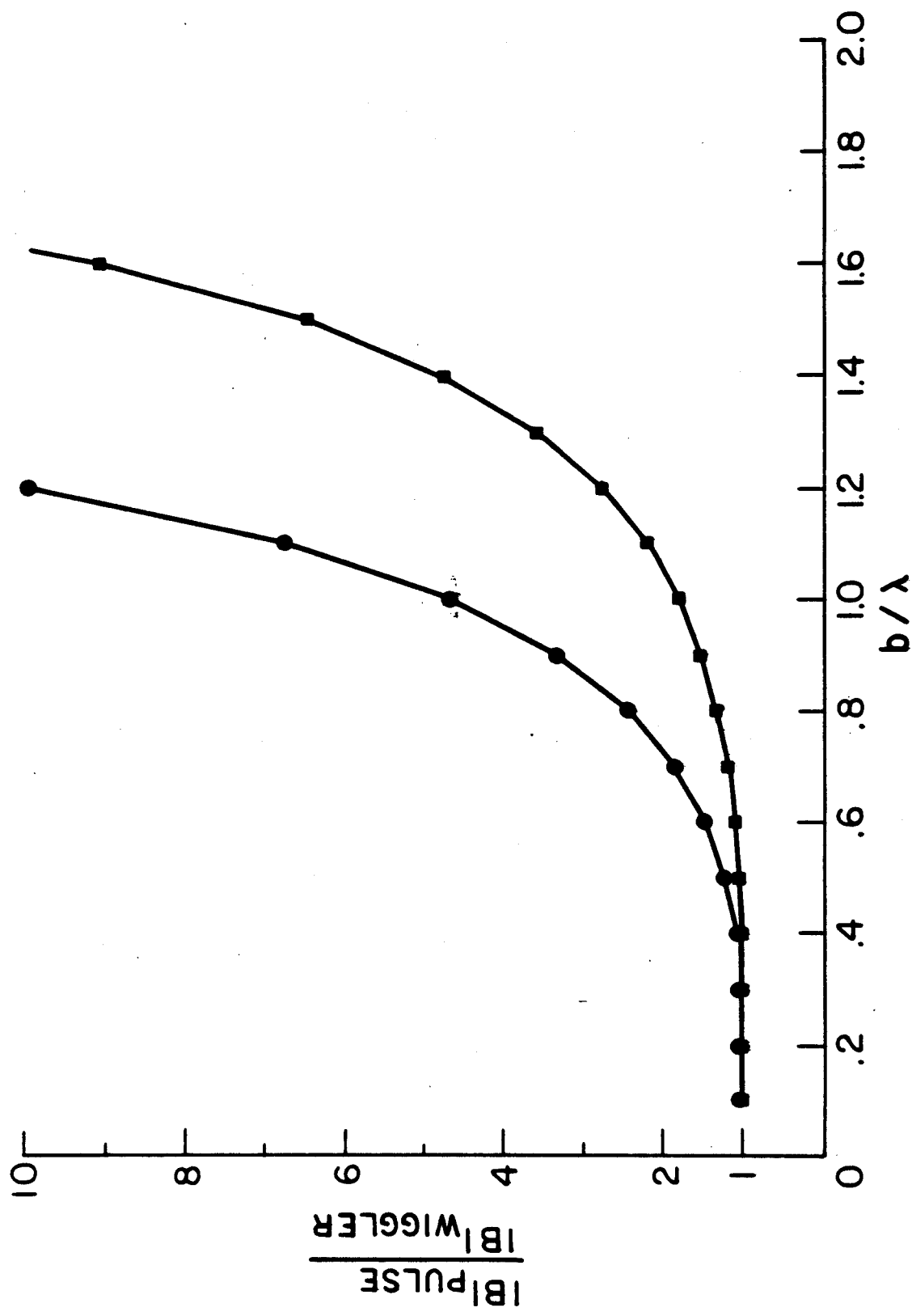


Fig. 8
Fajans

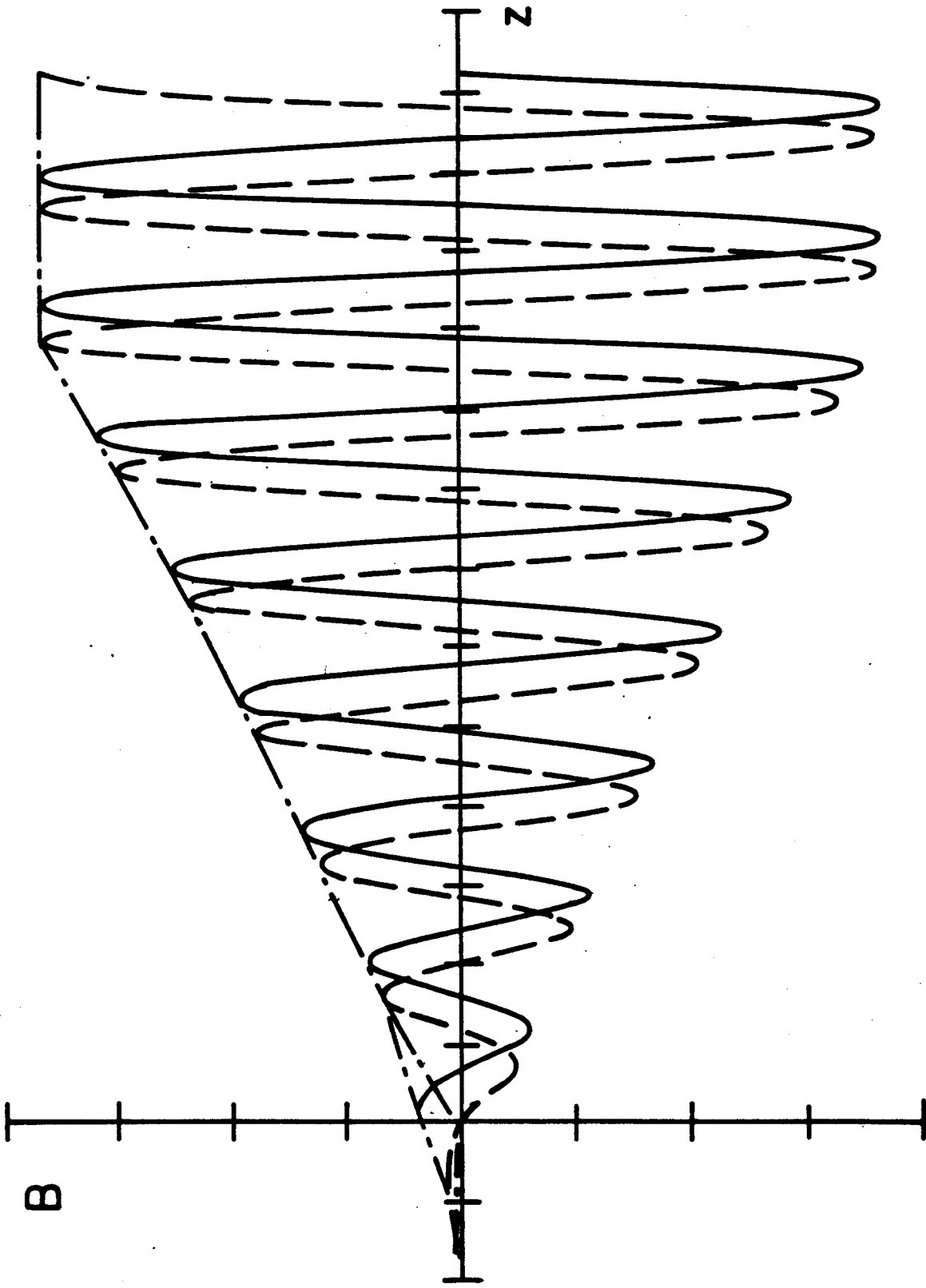


Fig. 9a
Fajans

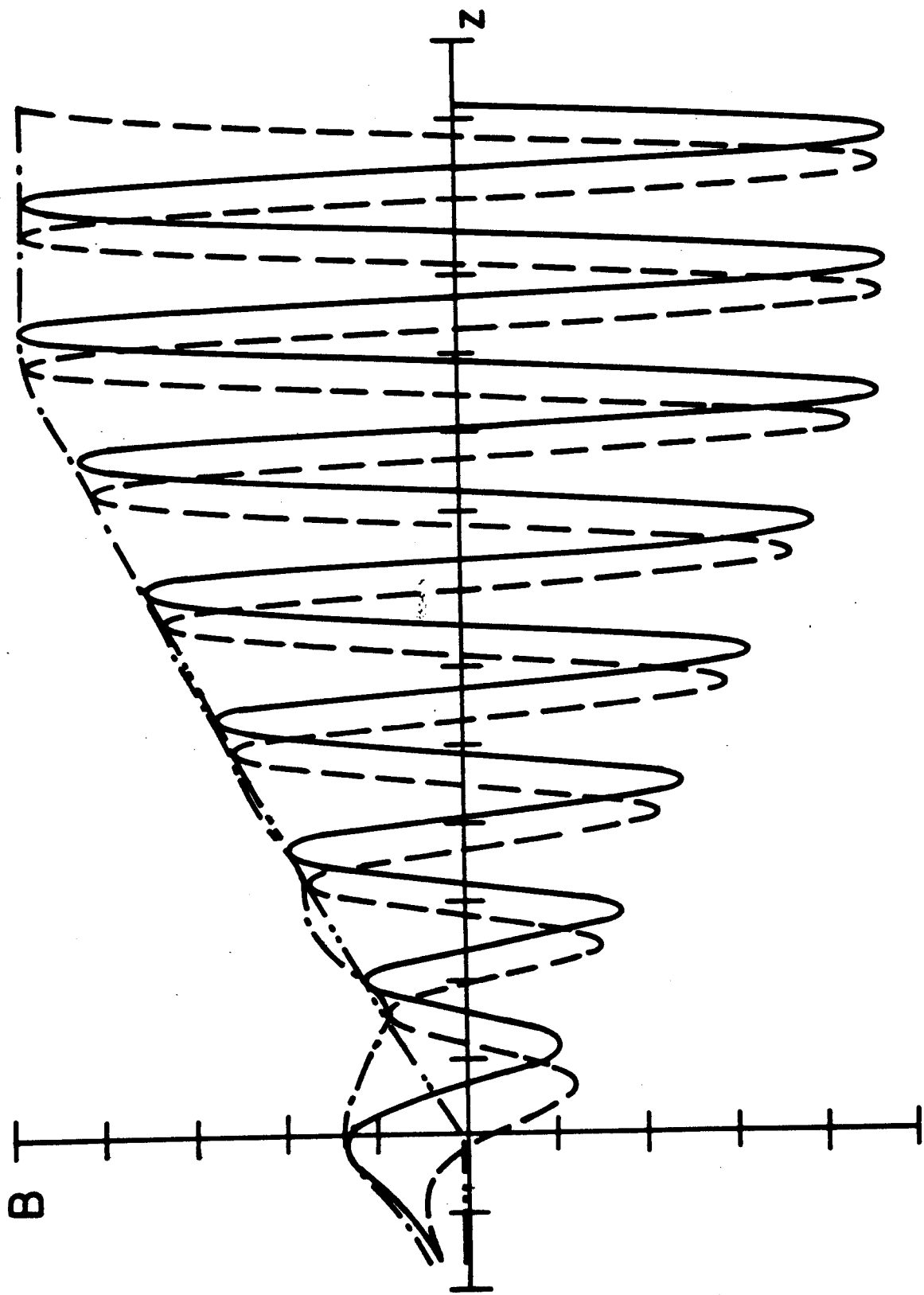


Fig. 9b
Fajans

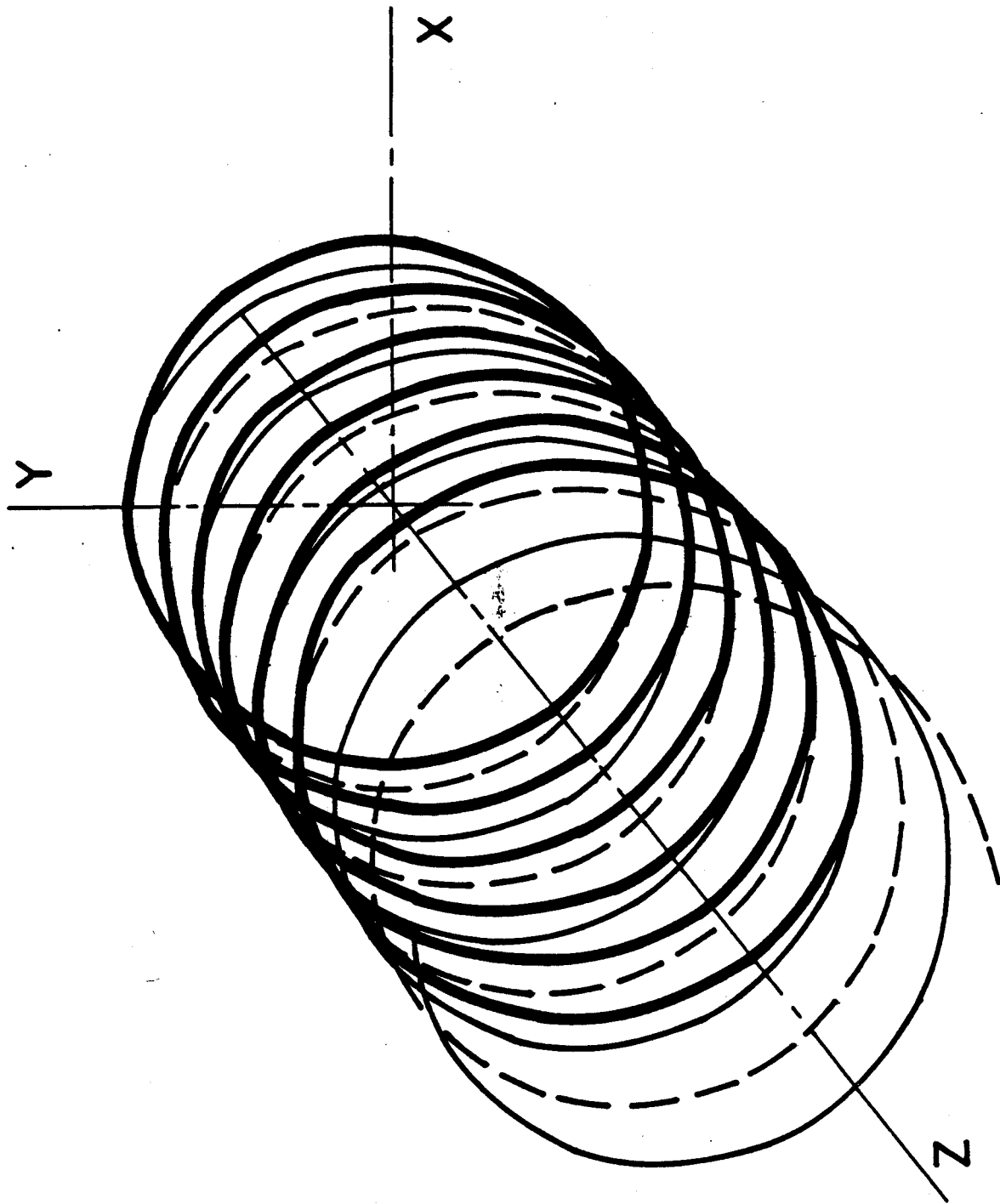


Fig. 10a
Fajans

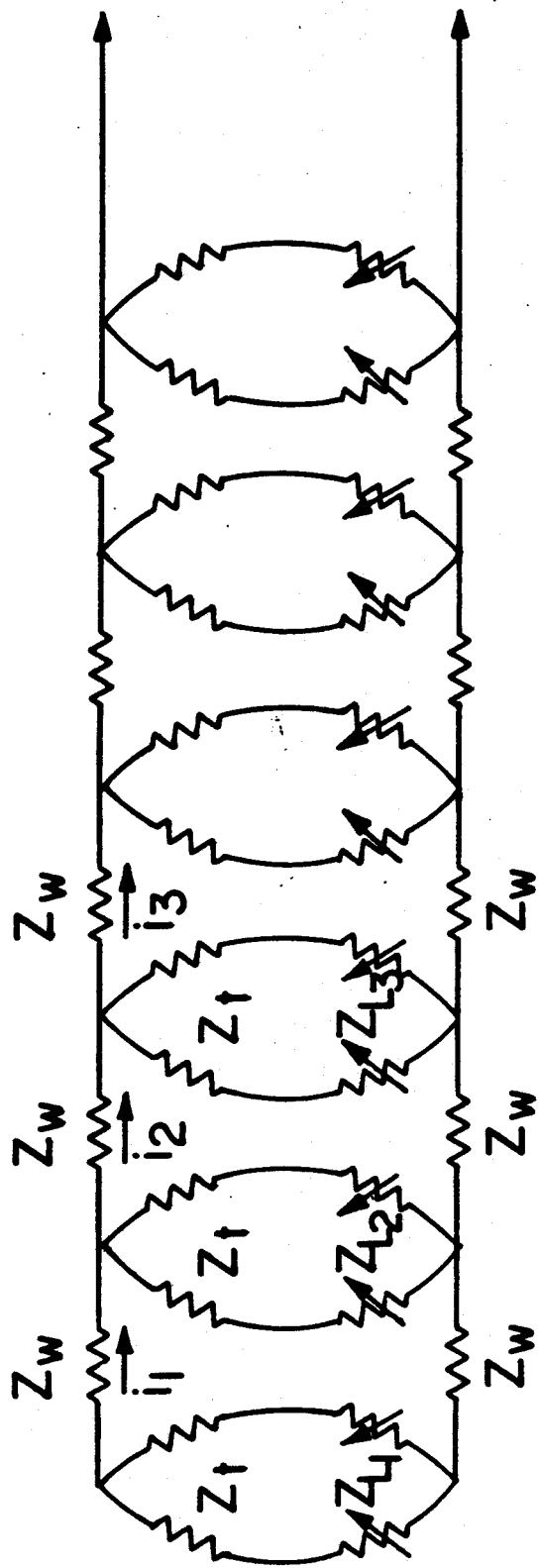


Fig. 10b
Fajans

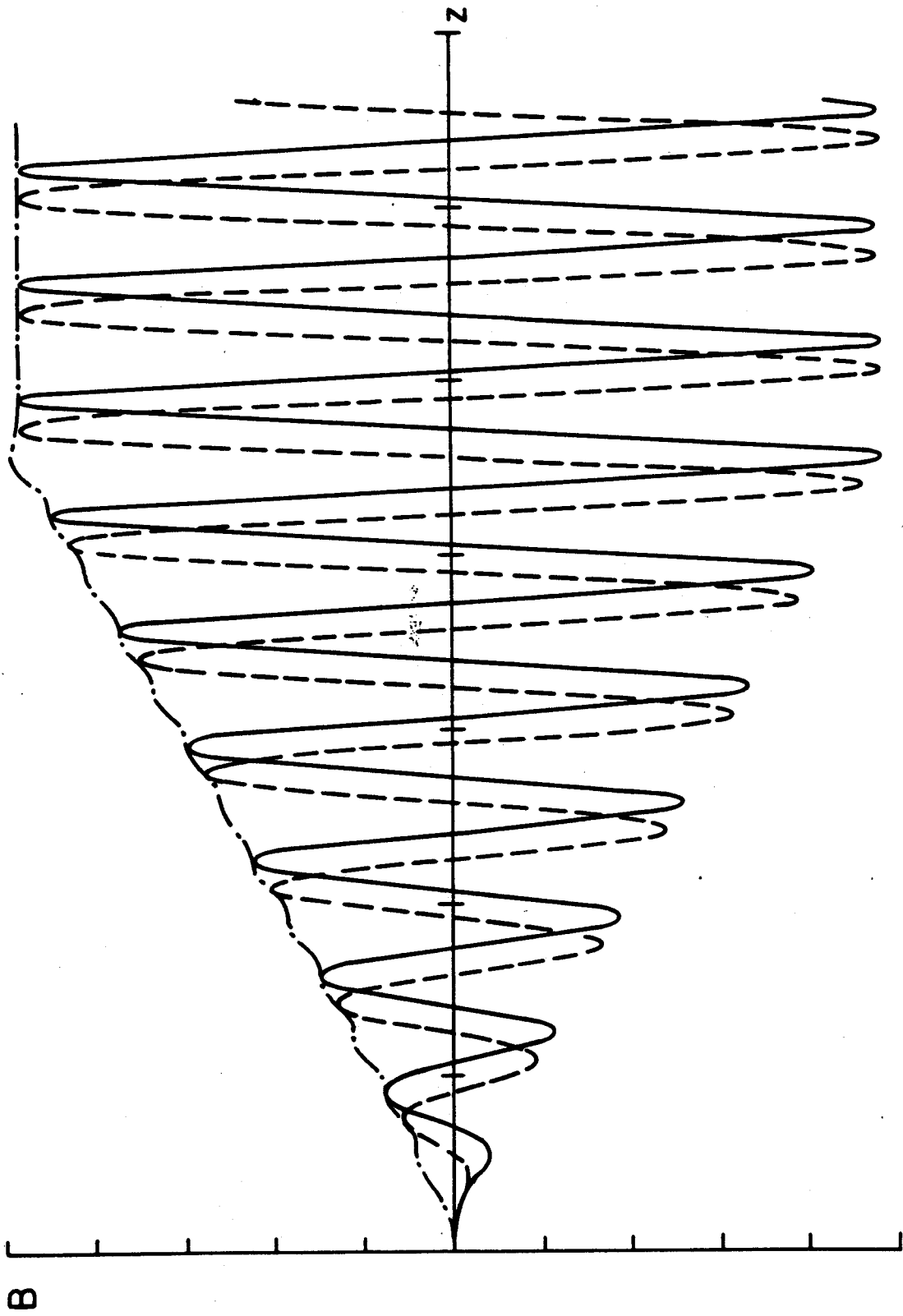


Fig. 11a
Fajans

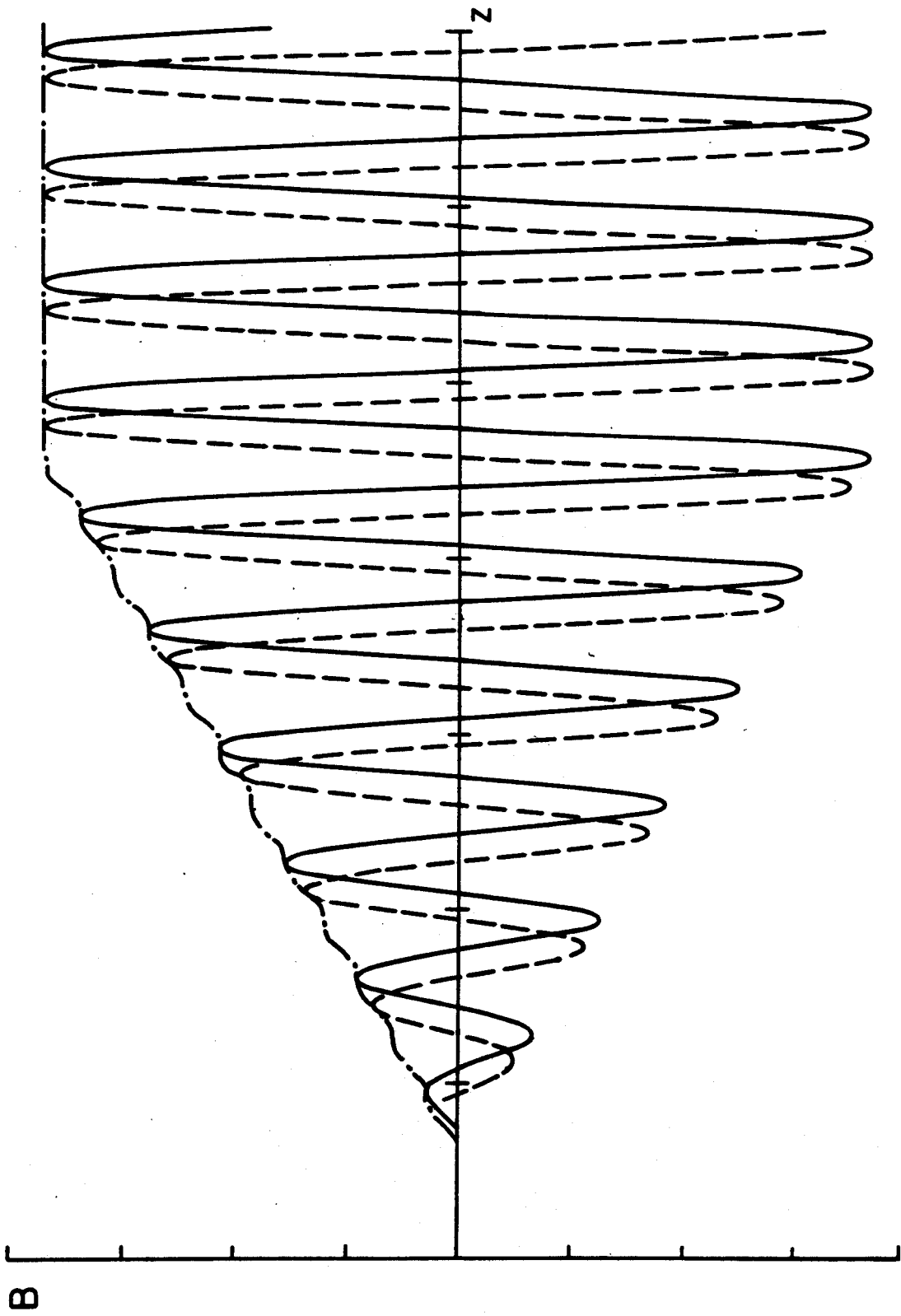


Fig. 11b
Fajans